

Semiclassical dynamics of a superconducting circuit: chaotic dynamics and fractal attractors

Davide Stirpe,¹ Juuso Manninen,² and Francesco Massel²

¹*Dipartimento di Scienza Applicata e Tecnologia, Politecnico di Torino,
Corso Duca degli Abruzzi 24, I-10129 Torino, Italy*

²*Department of Science and Industry Systems, University of South-Eastern Norway, PO Box 235, Kongsberg, Norway*
(Dated: March 31, 2023)

In this article, we study the semiclassical dynamics of a superconducting circuit constituted by two Josephson junctions in series, in the presence of a voltage bias. We show that the equations of motion describing the superconducting phase correspond to those controlling the dynamics of a planar rotor with an oscillating pivot and, consequently, to those of a Kapitza pendulum in the absence of gravity. In addition, we show that the system exhibits a rich dynamical behavior with chaotic properties and provide insight into its attractor's fractal nature.

I. INTRODUCTION

Superconducting circuits are arguably one of the most successful quantum computing platforms [1], exhibiting circuits of growing complexity (see e.g. [2]), for which early examples of quantum error correction have been recently demonstrated [3]. Their success relies essentially on the possibility of engineering circuit nonlinearities through the addition of Josephson junctions. While the specific topology of the circuit determines the difference between distinct designs—such as flux [4], phase [5] and transmon [6] qubits—an important parameter characterizing these devices is the ratio between the circuit changing energy (E_c) and the Josephson energy (E_J). The control of these two parameters allows experimenters to isolate, within the quantum-mechanical spectrum of the circuit, a two-level system: the qubit [7].

While the design of qubits requires the ability to control these nonlinearities at the “fully quantum” level (i.e. taking into account the quantization of energy levels), striking consequences of the tunneling between superconductors can already be identified at the semiclassical level. These include the Aharonov–Bohm effect [8] and definition of the voltage standard in terms of the Josephson effect [9].

In this article, we focus on the latter aspect. We describe the semiclassical dynamics of the superconducting phase in a circuit constituted by two Josephson junctions in series, in the presence of an external voltage bias. This setup (see Fig.1) defines a superconducting island coupled to the rest of the circuit by two (superconducting) tunnel junctions. This setting is analogous to a superconducting single-electron transistor (SSET) at zero-gate voltage. Our analysis, however, differs from the quantum analysis of SSETs inasmuch as we consider here a semiclassical description.

The range of validity of this description is, unsurprisingly, complementary to the one required to observe charge quantization in SETs [10] for which the condition $R_T \gg R_K$ —where R_T is the tunnel resistance of the circuit and $R_K = h/e^2$ is the resistance quantum—should hold. In our setup, for the semiclassical approximation

to be valid, we have to assume that $Z \ll R_K$, where $Z \propto \sqrt{E_c/E_J}$, is the characteristic impedance of the circuit.

With this picture in mind, we analyze here the dynamics of the system, recognizing how the equations of motion correspond to the dynamics of a planar pendulum, whose pivot is periodically driven. This system can, in turn, be regarded as a particular instance of the Kapitza pendulum [11] at zero gravity. In our work, we show that the dynamics leads to three types of attractors: stable and unstable points and cyclic orbits. The latter are limit cycles trajectories showing a multiple nodding feature. While this behavior was first considered in [12], its full characterization has not, to our knowledge, been carried out previously. Here, we give a complete account of the limit-cycle solutions in terms of their distinctive number of nodes. Furthermore, we investigate the distribution of the attractors as a function of two control parameters (voltage and initial phase on the island). We discover that the dynamics emerging from this system exhibits a rich and complex structure, revealing a chaotic behavior. We gain more insight on this aspect estimating the fractal dimensions of the different regions in the parameters space.

The paper is organized as follows: in Section II we derive the equations of motion for the circuit through a Hamiltonian description of the circuit [7, 13], establishing the analogy between our superconducting circuit and the dynamics of the driven rotor in Section III. In the end, we discuss in Section IV the numerical solution of the Equations of motion for different values of the system's parameters, examining the different types of trajectories and the nature of the attractors.

II. SEMICLASSICAL MODEL AND EQUATIONS OF MOTION

As anticipated, the system we are considering is a superconducting circuit constituted by two Josephson junctions in series, in the presence of a voltage bias V_g (see Fig. 1). The two Josephson junctions have Josephson ca-

capacitances C_{J1} and C_{J2} and Josephson energies E_{J1} and E_{J2} , respectively. While we initially focus on a purely reactive circuit model to derive a Hamiltonian description of the system, we subsequently introduce dissipation, which can be modelled introducing a resistive shunt for the two JJs, using the resistively and capacitively shunted junction (RCSJ) model [14]. The resistive shunt can, for instance, describe a quasiparticle contribution to the tunneling current.

The circuit topology described here is equivalent to the one describing superconducting single-electron transistors. However, a key distinction between our setting and a SSET is that, for the latter, the focus is on the so-called Coulomb blockade regime [10], allowing for charge quantization on the island. For a superconducting circuit, such regime is reached for $Z \gg R_K$, e.g. characteristic impedance larger than the resistance quantum. Here, as previously mentioned, we focus on the opposite situation ($Z \ll R_K$), in analogy to the strategy employed in the design of phase qubits [1, 5, 15]. This can be achieved by allowing the tunneling junctions to be large, even macroscopic, increasing their capacitance and thus lowering the charging energy $E_C \propto 1/C$ or, alternatively, adding a large shunting capacitance. A consequence of this is that the number of Cooper-pairs on the qubit island is no longer a good quantum number—like for SETs—and, instead, the phase dynamics becomes the dominating effect, allowing us to treat the superconducting phase across the junctions semiclassically.

As anticipated, we first consider our analytical mechanics description of our system, as shown in [13]. This allows for a straightforward quantization procedure which, however, is not the focus of our work. In order to form the Lagrangian and the Hamiltonian of the circuit, we largely follow [7, 13]. In particular, we use a specific procedure where the constraint on the external voltage is enforced in the Lagrangian by substituting the voltage source in Fig. (1) with a capacitance C_g . Taking then the limit $C_g \rightarrow \infty$ induces the gate voltage V_g on the lead g . The general approach consists in defining flux variables ϕ_i at each node of the circuit $i \in \{g, I, o\}$. The voltage V_i on each island is related to the flux by defining $\phi_i(t) = \int_{-\infty}^t dt' V_i(t')$, implying $V_i(t) = \dot{\phi}_i(t)$. Without loss of generality, we impose here $\dot{\phi}_o = 0$ for the grounded node. The inductive energy associated with the JJs gives the potential part of the Lagrangian $\mathcal{U}(\vec{\phi}) = -E_{J1} \cos\left(\frac{2\pi}{\Phi_0}(\phi_g - \phi_I)\right) - E_{J2} \cos\left(\frac{2\pi}{\Phi_0}\phi_I\right)$, where $\Phi_0 = h/(2e)$ is the flux quantum. Writing the standard capacitive energy as the kinetic term, we obtain the Lagrangian of the system $\mathcal{L} = \mathcal{L}(\vec{\phi}, \dot{\vec{\phi}}) = \frac{1}{2}\dot{\vec{\phi}}^T \mathcal{C} \dot{\vec{\phi}} - \mathcal{U}(\vec{\phi})$, where $\vec{\phi} = \begin{pmatrix} \phi_g \\ \phi_I \end{pmatrix}$ and $\mathcal{C} = \begin{pmatrix} C_{J1} + C_g & -C_{J1} \\ -C_{J1} & C_{J1} + C_{J2} \end{pmatrix}$ is the capacitance matrix. The Hamiltonian is straightforwardly expanded as the Legendre Transform of the La-

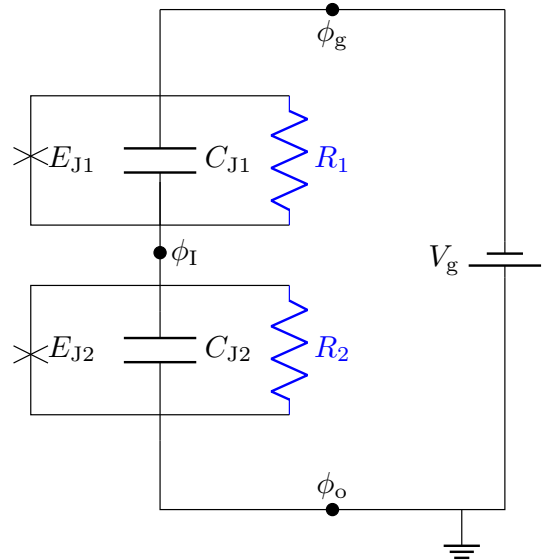


FIG. 1: Equivalent circuit for the device. Each Josephson junction consists of a capacitance and a non-linear inductance in parallel. To take account of possible dissipative phenomena, like for instance quasiparticle currents, we generalize the circuit introducing resistors (blue in the figure) in parallel to the capacitor and the inductor. The junctions are linked by means of the superconducting island (node I), while nodes g and o are superconductive leads. The system is voltage biased by an external voltage source V_g .

grangian ($\mathcal{H} = \sum_i Q_i \phi_i - \mathcal{L}$). Explicitly,

$$\begin{aligned} \mathcal{H} &= \frac{1}{2} \vec{Q}^T [\mathcal{C}]^{-1} \vec{Q} + \mathcal{U} = \\ &= 4E_C (n - \bar{n}_g)^2 - E_{J1} \cos(\varphi_g - \varphi_I) - E_{J2} \cos(\varphi_I), \end{aligned} \quad (1)$$

where $E_C = \frac{e^2}{2(C_{J1} + C_{J2})}$ is the qubit charging energy, $n = Q_I/(2e)$ is the number of Cooper pairs on the qubit island, $\bar{n}_g = -\frac{C_{J1}C_{J2}}{C_{J1} + C_{J2}} \frac{V_g}{2e}$ is the so-called gate charge and $\varphi_i = \frac{2\pi}{\Phi_0} \phi_i$, with $i = g, I$, are the flux-phase relation for the superconducting phase on the island I and on the lead g .

Here, by taking the limit $\lim_{C_g \rightarrow \infty} [\mathcal{C}]^{-1}$, we obtain the gate voltage on the lead g and the gate charge converges to $\bar{n}_g = -C_{J1}V_g/(2e)$.

The Hamilton's equations for the number of Cooper pairs and the phase on the qubit island are

$$\dot{n} = -\frac{1}{\hbar} \frac{\partial \mathcal{H}}{\partial \varphi_I} = \frac{E_{J1}}{\hbar} \sin(\varphi_g - \varphi_I) - \frac{E_{J2}}{\hbar} \sin(\varphi_I), \quad (2a)$$

$$\dot{\varphi}_I = \frac{1}{\hbar} \frac{\partial \mathcal{H}}{\partial n} = 8E_C(n - \bar{n}_g), \quad (2b)$$

giving the current and the voltage on the island, respectively.

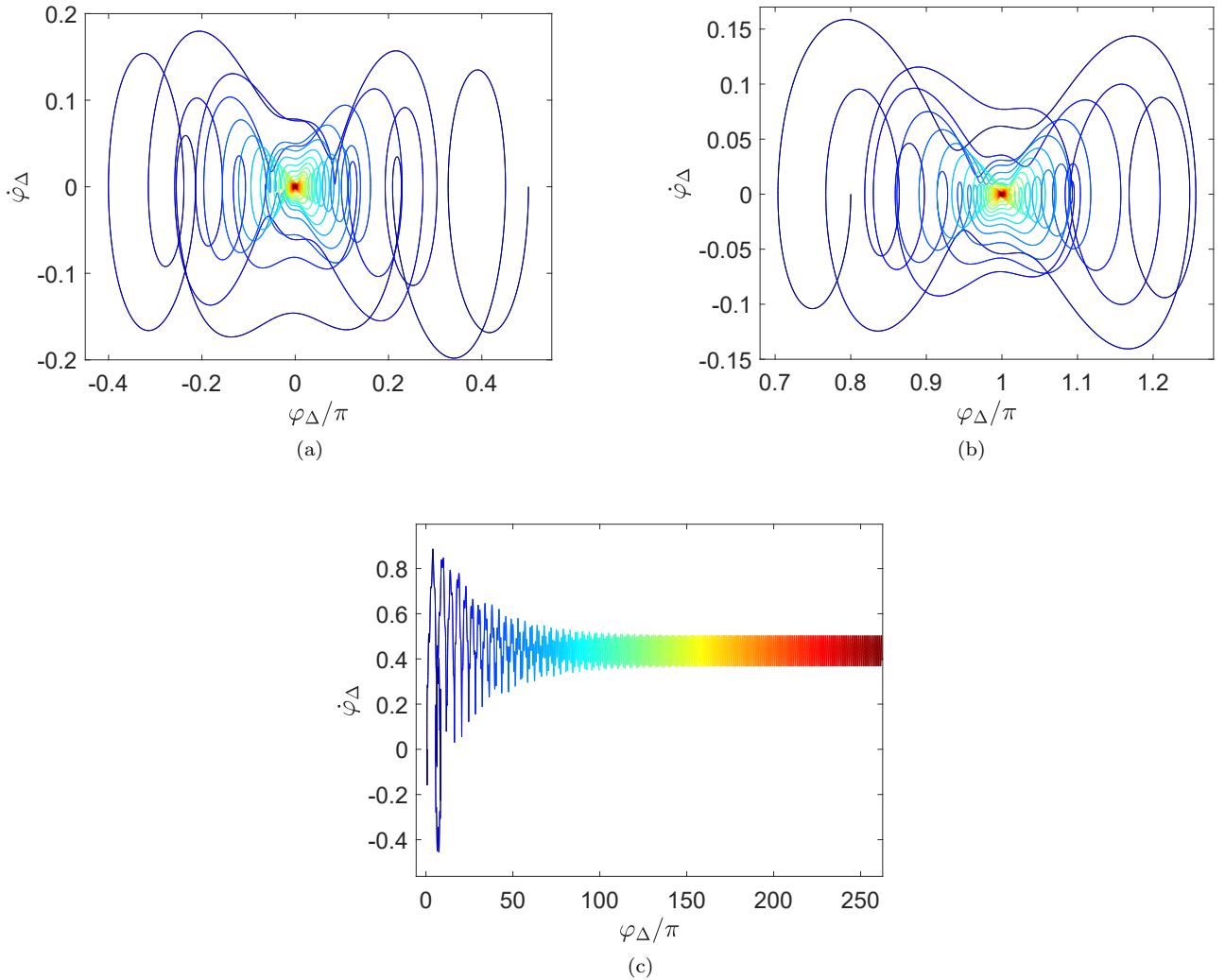


FIG. 2: Trajectories in the phase-space of two stable and one unstable solutions. For what concerns the stable solutions, they start from their respective initial conditions and the phase, in both cases, provides damped oscillation with decreasing amplitude: the trajectories, in the phase-space, are converging to their respective fixed points. The change in color of the plot from black to red indicates the direction of time in all the plots. (a) 0-stable solution for $\bar{\epsilon} = 0.27$ and $\varphi_{\Delta}(0) = 0.5\pi$. (b) π -stable solution for $\bar{\epsilon} = 0.27$ and $\varphi_{\Delta}(0) = 0.8\pi$. (c) Unstable solution for $\bar{\epsilon} = 0.58$ and $\varphi_{\Delta}(0) = 0.8\pi$, reported only in the initial instants of the solution. Here, the trajectory does not remain in a neighborhood of one of the fixed points. In the mechanical equivalent description, it is like the pendulum continues to constantly rotate, allowing the angle to exceed the range $[0, 2\pi]$.

Let us assume that the Josephson energies of the two junctions are identical, i.e. $E_{J1} = E_{J2} = E_J$. Differentiating Eq. (2b) with respect to time and substituting Eq. (2a) in it, we obtain

$$\ddot{\varphi}_{\Delta} = -2\Omega_J^2 \sin(\varphi_{\Delta}) \cos\left(\frac{\varphi_g}{2}\right), \quad (3)$$

where $\varphi_{\Delta} = \varphi_1 - \frac{\varphi_g}{2}$ and $\Omega_J = \frac{\sqrt{8E_C E_J}}{\hbar}$ is the Josephson frequency. Eq. (3) can be written in a dimensionless form as

$$\frac{\partial^2 \varphi_{\Delta}}{\partial \tau^2} = -\bar{\epsilon} \cos(\tau) \sin \varphi_{\Delta}, \quad (4)$$

where $\bar{\epsilon} = 8\frac{\Omega_J^2}{\omega_g^2}$, $\tau = \frac{\omega_g t}{2}$ and $\omega_g = \frac{2\pi V_g}{\Phi_0}$. See Appendix A and B for further details on the derivation of the system's Hamiltonian and EOMs.

Eq. (4), describing the time evolution of the phase difference φ_{Δ} , can be interpreted as the dynamical equation for a rigid planar rotor whose pivot oscillates -in the units of the Eq. (4)- with unit frequency. In turn, this system can be thought of as a zero-gravity Kapitza pendulum [11, 16].

We remark that our discussion has been so far limited as considering only the reactive part of the circuit.

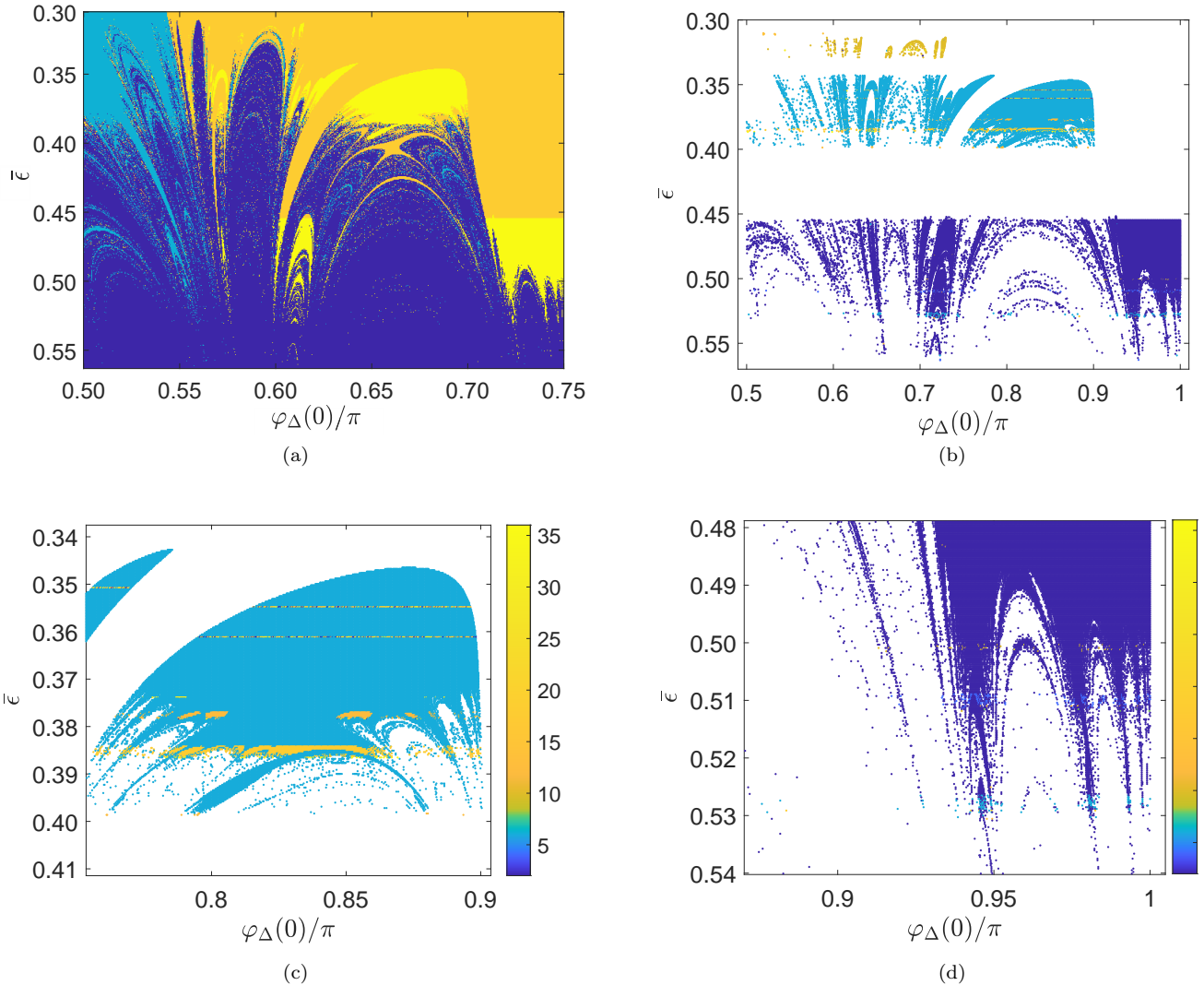


FIG. 3: (a) Classification of the space of the parameters for 896×2048 points for $\varphi_{\Delta} \in [\frac{\pi}{2}, \pi]$ in the horizontal axis and $\bar{\epsilon} \in [0.3, 0.58]$ in the vertical axis. The space is divided into four regions by the attractors, each of them labelled by a different color: dark blue stands for unstable, light blue for 0-stable, orange for π -stable and yellow for limit cycle solutions. (b) Classification in terms of number of nodes of the limit cycle solutions, labelled in yellow in the Fig. 4a. The most recurring numbers of nodes are 2 (blue), 6 (green) and 10 (yellow), each of them occurring in three divided subregions. However, the limit cycle solutions exhibit stripes for some specific values of $\bar{\epsilon}$ in which more complex cycle limit structure are found. (c)-(d) are two different insets where it is possible to see stripes of 9-cycle solutions. For $\bar{\epsilon} = 0.354838865, 0.361176755$ two narrow stripes with a large variety of n -cycle are detected.

See Section III and Appendix C for a lumped element description of the resistive contribution.

III. SUPERCONDUCTING CIRCUIT AND THE KAPITZA PENDULUM

The dynamical equation controlling the Kapitza pendulum can be written as

$$\ddot{\theta} = -[\alpha \cos(\omega t) + g] \sin(\theta) - \eta \dot{\theta}, \quad (5)$$

where the term $g \sin(\theta)$ describes the gravity exerted on the rotor, whereas the cosinusoidal term, with amplitude α and frequency ω , describes the pivot's oscillation. The term $\eta \dot{\theta}$ models the friction experienced by the rotor. All the previous parameters play a crucial role in the dynamical properties of the pendulum and, in principle, the latter can largely differ from the case of a simple pendulum without vertical driving. In fact, for some particular conditions the inverted position, corresponding to the angle $\theta = \pi$, becomes a stable fixed point, unlike the simple pendulum case. Interesting results concerning the stabilization of the inverted position

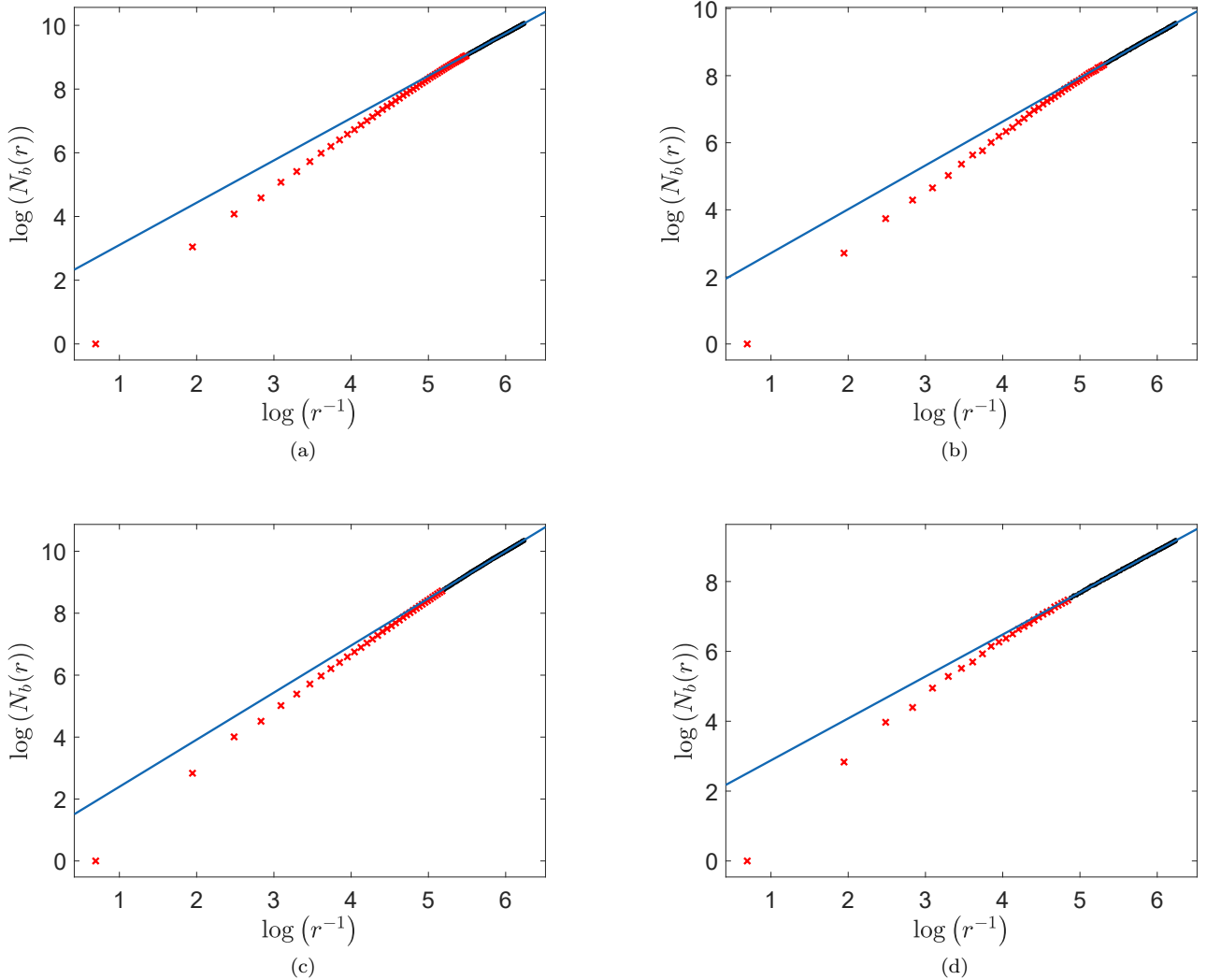


FIG. 4: Determination of the fractal dimensions via linear best fits (blue lines) of the four different regions in Fig. 3a. The box counting method implemented here consists in iteratively halving the length r of the boxes and counting the number of boxes covering the border of each region $N_b(r)$. After this, the Hausdorff's dimension δ_H is obtained as the angular coefficient of the line fitting the rightmost data on the logarithmic plane $\log(r^{-1})$ - $\log(N_b(r))$. (a) 0-stable solutions, $[\log(N_b(r))] = 1.327 [\log(r^{-1})] + 1.778$. (b) π -stable solutions, $[\log(N_b(r))] = 1.307 [\log(r^{-1})] + 1.402$. (c) unstable solutions, $[\log(N_b(r))] = 1.520 [\log(r^{-1})] + 0.876$. (d) Cycle limit solutions $[\log(N_b(r))] = 1.201 [\log(r^{-1})] + 1.679$.

of the driven pendulum have been obtained, decomposing the motion in slow and fast component [16]. A more rigorous analytical treatment was provided in [11], where the parameters region leading to the stabilization of the inverted pendulum were identified. In addition, further numerical simulations have shown that the stabilization of the upward direction has been obtained in presence of small friction [17]. Other different types of attractors, like limit-cycle trajectories, have been found in the case of the Kapitza pendulum with gravity. The structure and the periodicity of these regular orbits in the phase-space strongly depend on the parameters. In particular,

a multiple-nodding description of limit-cycle trajectories is suggested in [12], where the expression n -nodding refers to trajectories in which an observer, moving as the oscillating pivot, detects a trajectory which nods n times on both the left and the right side of the fixed points 0 or π . For the sake of the simplicity, in this work we recall a n -nodding limit-cycle (or simply n -cycle) a phase space $(\varphi_\Delta, \dot{\varphi}_\Delta)$ periodic trajectory that crosses the $\dot{\varphi}_\Delta = 0$ axis $2n$ times (see Figs. 6-9 and Appendix C).

In our case, the dissipation can be taken into account through the RCSJ model for JJs [14]. Thus, Eq. (4)

becomes

$$\ddot{\varphi}_{\Delta} = -\bar{\epsilon} \cos(\tau) \sin \varphi_{\Delta} - \gamma \dot{\varphi}_{\Delta}, \quad (6)$$

where the time derivatives are taken with respect to τ and the dimensionless dissipation term is $\gamma = \frac{2}{\omega_{\bar{g}}} \frac{2}{R(C_{J1} + C_{J2})}$. Here R describes the resistance used to model the losses in the RCSJ context. We see that this expression generalizes Eq. (4) for nonzero losses, where the damping rate is given by $\frac{1}{RC_J}$ for junctions with equal Josephson capacitances $C_{J1} = C_{J2} = C_J$. See Appendix C for the derivation of the dissipative part of our model.

The analogy between Eqs. (5) and (6) demonstrates the correspondence between the mechanical description of the Kapitza pendulum and the semiclassical treatment of the circuit considered here. In terms of this correspondence, the initial condition for the superconducting phase of the lead, $\varphi_{\bar{g}}(0) = 0$, corresponds to choosing the initial pivot angle as the reference point. Since $\varphi_{\Delta} = \varphi_I - \frac{\varphi_{\bar{g}}}{2}$, imposing initial condition on the phase φ_{Δ} coincides with imposing initial condition on the island phase, which, in turn, corresponds to setting superconducting current through the island I at $t = 0$.

In the following section, we obtain that the dynamics of Eq. (6) is mainly described by the four types of attractors already discussed— 0 , π stable, unstable and limit-cycle solutions—but we get a complete description of the parameters space (composed by φ_{Δ} and $\bar{\epsilon}$) with respect to these four attractors. Concerning the limit-cycle solutions, we obtain, in the terminology of Ref. [12], a rich picture of multiple-nodding trajectories, including double- and triple-nodding solutions. Following our definition, 1-cycle and 3-cycles were analyzed and represented in the phase-space in [12], along with a cursory mention of the existence of 4-cycles as possible solutions of Eq. (5). Here, in addition to these results, we reveal also limit-cycles characterized by more complex structures and by an unexpected total number of nods, characterizing the distribution and the fractal behaviour of the attractors in the parameters space, something not yet observed and studied, as far as we know: as an example, we find 5-cycle, 9-cycle and 15-cycle solutions). We plot the phase-space portraits of the 5-cycle and 9-cycle solutions in Figs. 8-9. Furthermore, we classify the different points of the phase space, in terms of the attractors. This classification leads to the division of the parameters space in distinctive regions (see Figs. 3) showing sensitivity to the values of the parameters and, consequently, a chaotic behavior. In order to characterize this last aspect, we estimate the Hausdorff's dimension of the different attractors regions.

IV. NUMERICAL RESULTS

Having established that the general form of the dynamics of φ_{Δ} corresponds to the dynamics of a mechanical planar rotor with an oscillating pivot, we focus here on

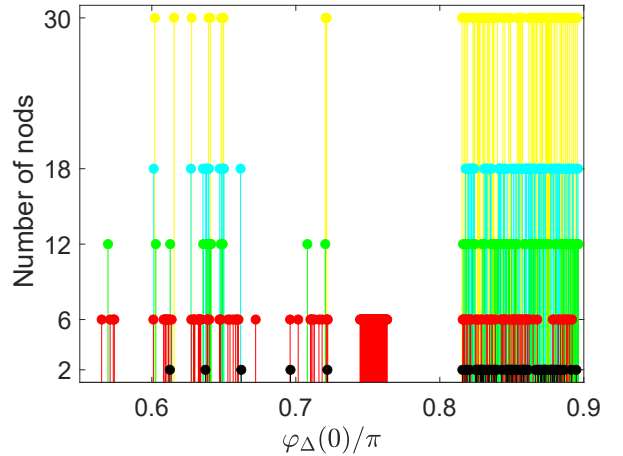


FIG. 5: The distribution of the numbers of nods in terms of the phase φ_{Δ} is shown in correspondence to the stripe emerging for $\bar{\epsilon} = 0.354838865$. The latter is quite similar to the distribution obtained for the stripe for $\bar{\epsilon} = 0.361176755$.

the numerical investigation of the system's dynamics as a function of the driving amplitude and initial value of φ_{Δ} ($\bar{\epsilon}$ and $\varphi_{\Delta}(0)$, respectively).

As formerly discussed, through the numerical simulations we derive the already mentioned stability properties of the Kapitza pendulum (in the case of zero gravity) [11, 12, 16, 17], like the presence of stable fixed point $\varphi_{\Delta} = 0, \pi$ and limit-cycles. However, our analysis depicts a richer dynamical scenario in which we characterize the distribution of the attractors and, in addition, we describe the nature of the multiple-nodding behavior of the limit cycle trajectories in terms of their characteristic number of nods, giving emphasis to their distribution with respect to the parameters. In this work, the solutions are generated for a certain value of the initial phase $\varphi_{\Delta}(0) \in [\frac{\pi}{2}, \pi]$ and $\bar{\epsilon} \in [0.01, 0.60]$. From the plots of the solutions in the phase-space, we deduce that a very rich dynamical picture emerges, finding four different types of attractors:

- damped oscillations around $\varphi_{\Delta}(0) = 0$, i.e. $\varphi_{\Delta} = 0$ is a stable point (see Fig. 2a);
- damped oscillations around $\varphi_{\Delta}(0) = \pi$, i.e. $\varphi_{\Delta} = \pi$ is a stable point (see Fig. 2b);
- trajectories in which the phase grows in time and no fixed point is reached, i.e. unstable solutions (see Fig. 2c);
- periodic and stable trajectories around $\varphi_{\Delta} = 0$ or $\varphi_{\Delta} = \pi$, reached after a transient damped oscillation i.e. solutions stabilizing in a limit-cycle (see Figs. 6-9).

The classification of the attractors for parameters space enclosed within $\bar{\epsilon} \in [0.3, 0.58]$ and $\varphi_{\Delta}(0) \in [\frac{\pi}{2}, \pi]$

is shown in Fig. 3a, from which it is straightforward to see that the attractors divide the space of the parameters in four distinct stability regions — 0, π stable, unstable points and limit cycles— with a strong sensitivity to initial conditions. We characterize the Hausdorff's (or fractal) dimensions of these regions, estimating them with the box counting method [18] and Linear Regression from the plots in Fig. 4: the dimension for limit-cycles is 1.201 ± 0.004 , 1.327 ± 0.007 for 0-stable, 1.307 ± 0.006 for π -stable and 1.520 ± 0.006 for unstable solutions.

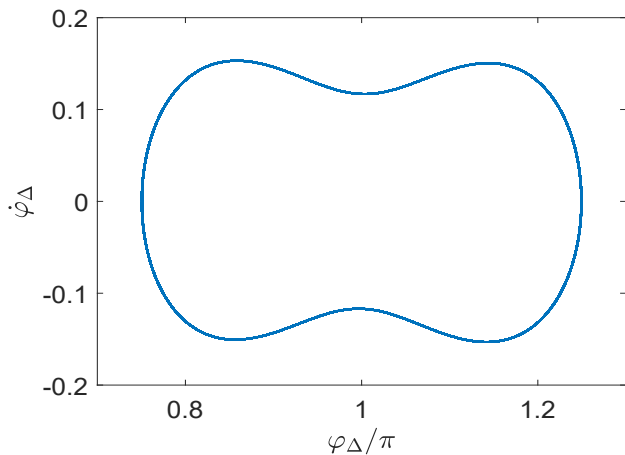


FIG. 6: 1-cycle solution for $\bar{\epsilon} = 0.5$ and $\varphi_{\Delta}(0) = 0.7\pi$.

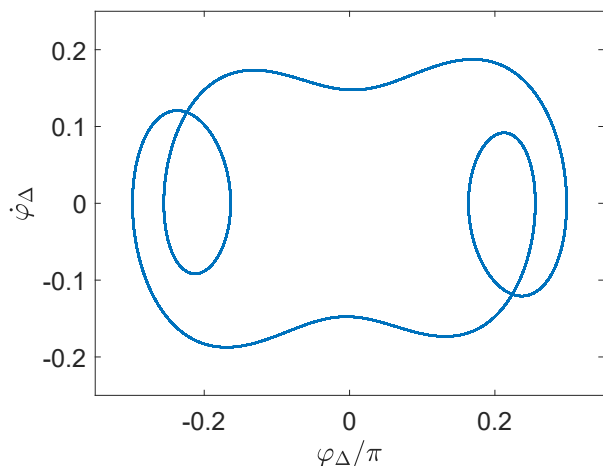


FIG. 7: 3-cycle solution for $\bar{\epsilon} = 0.37$ and $\varphi_{\Delta}(0) = 0.54\pi$.

Furthermore, the limit-cycles region (labelled in yellow in Fig. 3a) comprises different multiple-nodding trajectories, as shown in Fig. 3b, where the n -cycle solutions are classified in terms of the number of nodes $2n$. Here, it is straightforward to see that 1-cycle, 3-cycle and 5-cycle solutions (example of these solutions in the phase-space are shown in Figs. 6-8, respectively) divide

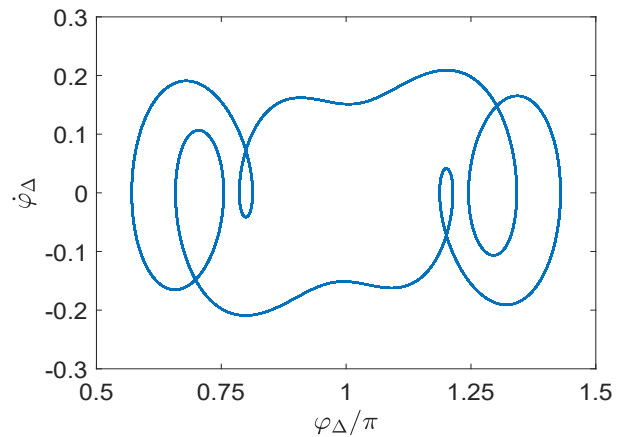


FIG. 8: 5-cycle solution for $\bar{\epsilon} = 0.318828$ and $\varphi_{\Delta}(0) = 0.727783\pi$.

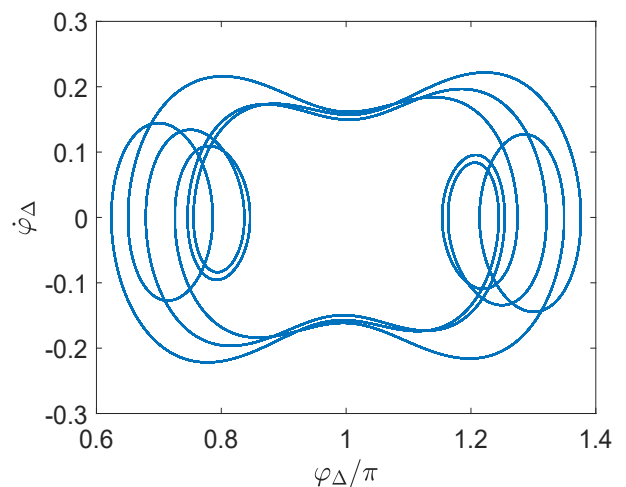


FIG. 9: 9-cycle solution for $\bar{\epsilon} = 0.385088$ and $\varphi_{\Delta}(0) = 0.827393\pi$.

the main limit-cycle region in three main subregions, with the emergence, however, of more complicated structure, for instance 9-cycle (phase-space trajectory in Fig. 9). Figs. 3c-3d show the emergence, for some specific values of the parameter $\bar{\epsilon}$, of stripes of limit-cycles characterized by an unusual distribution, some of them characterized by a surprisingly high number of nodes. As an example, for $\bar{\epsilon} = 0.354838865$ a stripe with a large variety of numbers of nodes emerges, whose distribution as a function of the phase φ_{Δ} is depicted in Fig. 5. The complete list of different n -cycle observed in our simulations is reported in Table I, where for each type of n -cycle solution the total number of nodes $2n$, its absolute and relative frequencies are indicated. Since each n -cycle generates a specific region in the parameters space, we estimate their fractal dimensions:

- 1.182 ± 0.124 for 2-cycle;

- 0.870 ± 0.184 for 4-cycle;
- 1.304 ± 0.110 for 6-cycle;
- 1.026 ± 0.056 for 10-cycle;
- 0.728 ± 0.282 for 12-cycle;
- 0.323 ± 0.100 for 14-cycle;
- 0.952 ± 0.126 for 18-cycle;
- 20-cycle and 22-cycle are point-like regions, so their dimensions are practically 0;
- 0.503 ± 0.015 for 30-cycle;
- 0.44 ± 0.093 for 36-cycle.

See Appendix D for more details about the estimation of the fractal dimensions and about procedures used for the characterization of the limit-cycle solutions.

TABLE I: Number of nodes, absolute frequency and %-frequency encountered in the analysis of the limit-cycles.

Number of nodes	Absolute frequency	Relative Frequency
2	49.58	73915
4	0.20	294
6	47.14	70279
8	0.01	14
10	0.89	1325
12	0.58	870
14	0.01	16
18	1.33	1985
20	0.001	2
22	0.001	1
30	0.21	326
36	0.03	46

V. CONCLUSIONS

We have shown that the superconducting phase across Josephson junctions in a simple geometry of two Josephson junctions in series behaves analogous to the zero gravity classical Kapitza pendulum. We identify four different types of stable solutions, accessible by tuning the gate voltage bias of the circuit. In particular, we find that the stable limit-cycle solutions can have a nontrivial multiple-nodding behavior, finding out a rich and diversified scenario of cyclic solutions characterized by unforeseen total number of nodes and complex structure in the phase-space. In addition, we describe the distribution of the attractors in the parameters space, from which we reveal the chaotic behavior of the system dynamics. We characterize the different solution spaces based on their Hausdorff dimensions and find them to be fractal with $\delta_H \sim 0.4 - 1.5$ depending on the type of the solution.

ACKNOWLEDGMENTS

FM and JM acknowledge financial support from the Research Council of Norway (Grant No. 333937) through participation in the QuantERA ERA-NET Cofund in Quantum Technologies (project MQSens) implemented within the European Union's Horizon 2020 Programme. The computations were performed on resources provided by Sigma2 - the National Infrastructure for High Performance Computing and Data Storage in Norway.

Appendix A: Deriving the Lagrangian and the Hamiltonian

We formulate the Lagrangian in terms of $\phi_i(t)$ and $\dot{\phi}_i(t) = V_i(t)$ associated to the nodes $i = g, I, o$, where the flux is taken as a coordinate-like variable. Due to the grounding of the circuit, we impose $\phi_o = 0$. In order to enforce the constraint of the external voltage $V_g = \dot{\phi}_g$ in the Lagrangian, we substitute the voltage source with a capacitance C_g , taking, in the end, the limit $C_g \rightarrow \infty$ [7]. The kinetic term takes the form

$$\mathcal{T} = \frac{1}{2} \vec{\dot{\phi}}^T \mathcal{C} \vec{\dot{\phi}} = \frac{1}{2} C_g \dot{\phi}_g^2 + \frac{1}{2} C_{J1} (\dot{\phi}_g - \dot{\phi}_I)^2 + \frac{1}{2} C_{J2} \dot{\phi}_I^2, \quad (\text{A1})$$

where \mathcal{C} is the capacitance matrix

$$\mathcal{C} = \begin{pmatrix} C_{J1} + C_g & -C_{J1} \\ -C_{J1} & C_{J1} + C_{J2} \end{pmatrix} \quad (\text{A2})$$

and $\vec{\dot{\phi}} = \begin{pmatrix} \dot{\phi}_g \\ \dot{\phi}_I \end{pmatrix}$.

The Lagrangian $\mathcal{L} = \mathcal{L}(\vec{\phi}, \vec{\dot{\phi}})$ is $\mathcal{L} = \frac{1}{2} \vec{\dot{\phi}}^T \mathcal{C} \vec{\dot{\phi}} - \mathcal{U}$, where the potential part is $\mathcal{U} = -E_{J1} \cos\left(\frac{2\pi}{\Phi_0}(\phi_g - \phi_I)\right) - E_{J2} \cos\left(\frac{2\pi}{\Phi_0}\phi_I\right)$. The charge Q_g on the lead g and Q_I on the island I are the momenta conjugated to the flux, easily obtained by the Lagrangian

$$\vec{Q} = \vec{\nabla}_{\dot{\phi}} \mathcal{L} = \begin{pmatrix} \frac{\partial \mathcal{L}}{\partial \dot{\phi}_g} \\ \frac{\partial \mathcal{L}}{\partial \dot{\phi}_I} \end{pmatrix} = \mathcal{C} \vec{\dot{\phi}} \quad (\text{A3})$$

Thus, the Hamiltonian $\mathcal{H} = \mathcal{H}(\vec{Q}, \vec{\phi})$ takes the form

$$\mathcal{H} = \vec{\dot{\phi}}^T \vec{Q} - \mathcal{L} = \frac{1}{2} \vec{Q}^T [\mathcal{C}]^{-1} \vec{Q} + \mathcal{U}, \quad (\text{A4})$$

where $[\mathcal{C}]^{-1}$ is the inverse capacitance matrix

$$[\mathcal{C}]^{-1} = \begin{pmatrix} \frac{1}{C_{J1}} & \frac{1}{C_{J12}} \\ \frac{1}{C_{J12}} & \frac{1}{C_{J2}} \end{pmatrix}, \quad (\text{A5})$$

written in terms of the quantities

$$\frac{1}{C_{11}} = \frac{C_{J1} + C_{J2}}{C_{J1}C_{J2} + C_g(C_{J1} + C_{J2})}, \quad (\text{A6})$$

$$\frac{1}{C_{12}} = \frac{C_{J1}}{C_{J1}C_{J2} + C_g(C_{J1} + C_{J2})}, \quad (\text{A7})$$

$$\frac{1}{C_{22}} = \frac{C_{J1} + C_g}{C_{J1}C_{J2} + C_g(C_{J1} + C_{J2})}. \quad (\text{A8})$$

Explicitly,

$$\mathcal{H} = \frac{1}{2C_{11}}Q_g^2 + \frac{1}{2C_{22}}Q_I^2 + \frac{1}{C_{12}}Q_gQ_I + \mathcal{U}. \quad (\text{A9})$$

Introducing the nominal bias voltage $V_g = \frac{Q_g}{C_{11}}$ and recalling $n = \frac{Q_I}{2e}$ the Hamiltonian takes the final expression

$$\mathcal{H} = 4E_{C_{22}}(n - \bar{n}_g)^2 + \frac{1}{2} \frac{C_{11}C_{22}}{C_{12}}V_g^2 + \mathcal{U}, \quad (\text{A10})$$

where $\bar{n}_g = -\frac{C_{11}C_{22}}{C_{12}}\frac{V_g}{2e}$ and $E_{C_{22}} = \frac{e^2}{2C_{22}}$.

In the limit of $C_g \rightarrow \infty$, the quantities defined above become

$$\frac{1}{C_{11}} \rightarrow 0, \quad (\text{A11})$$

$$\frac{1}{C_{12}} \rightarrow 0, \quad (\text{A12})$$

$$\frac{1}{C_{22}} \rightarrow \frac{1}{C_\Sigma} = \frac{1}{C_{J1} + C_{J2}}, \quad (\text{A13})$$

$$E_{C_{22}} \rightarrow E_C = \frac{e^2}{2C_\Sigma} = \frac{e^2}{2(C_{J1} + C_{J2})}, \quad (\text{A14})$$

and, as a consequence, the gate charge \bar{n}_g remains finite

$$\bar{n}_g \rightarrow -\frac{C_1}{2e}V_g, \quad (\text{A15})$$

whereas the second term in Eq. (A10) diverges. However, this energy contribution is constant, since it does not depend on the conjugated variables. Thus, it can be interpreted as a constant shift in the energy and, for this reason, it is neglected.

The final form of the Hamiltonian is

$$\begin{aligned} \mathcal{H} = & 4E_{C_\Sigma}(n - \bar{n}_g)^2 \\ & - E_{J1} \cos\left[\frac{2\pi}{\Phi_0}(\phi_g - \phi_I)\right] - E_{J2} \cos\left(\frac{2\pi}{\Phi_0}\phi_I\right). \end{aligned} \quad (\text{A16})$$

Appendix B: Deriving the Hamilton's equations and the dynamical equation for superconductive phase

The canonical conjugate variables in our formalism are the flux $\phi_i(t)$ and the charge $Q_i(t)$ at each node $i = g, I$. However, in this case, we write the Hamiltonian in terms

of the number of Cooper pairs $n_i = \frac{Q_i}{2e}$ and the phase $\varphi_i = 2\pi\frac{\phi_i}{\Phi_0}$. For this reason, taking f and g as two generic functions of the canonical variables, the usual Poisson brackets become

$$\{f, g\} = \sum_{i=g, I} \frac{\partial f}{\partial \phi_i} \frac{\partial g}{\partial Q_i} - \frac{\partial f}{\partial Q_i} \frac{\partial g}{\partial \phi_i} = \quad (\text{B1})$$

$$= \frac{1}{\hbar} \sum_{i=g, I} \frac{\partial f}{\partial \varphi_i} \frac{\partial g}{\partial n_i} - \frac{\partial f}{\partial n_i} \frac{\partial g}{\partial \varphi_i}, \quad (\text{B2})$$

from which we derive the Hamilton's equations for the variables at nodes $i = g, I$

$$\dot{n}_i = \{n_i, \mathcal{H}\} = -\frac{1}{\hbar} \frac{\partial \mathcal{H}}{\partial \varphi_i}, \quad (\text{B3})$$

$$\dot{\varphi}_i = \{\varphi_i, \mathcal{H}\} = \frac{1}{\hbar} \frac{\partial \mathcal{H}}{\partial n_i}. \quad (\text{B4})$$

Explicitly,

$$\begin{cases} \dot{n}_g = -\frac{E_{J1}}{\hbar} \sin(\varphi_g - \varphi_I) \\ \dot{n}_I = \dot{n} = \frac{E_{J1}}{\hbar} \sin(\varphi_g - \varphi_I) - \frac{E_{J2}}{\hbar} \sin(\varphi_I) \end{cases} \quad (\text{B5})$$

and

$$\begin{cases} \dot{\varphi}_g = \frac{2\pi}{\Phi_0} V_g \\ \dot{\varphi}_I = \frac{8E_{C_\Sigma}}{\hbar} (n - \bar{n}_g), \end{cases} \quad (\text{B6})$$

where the first equation in Eq. (B6) come from the constraint on the external voltage V_g . Thus, its integration leads to the expression for the phase in the superconductive lead

$$\varphi_g(t) = \varphi_g(0) + \omega_g t, \quad (\text{B7})$$

where $\omega_g = \frac{2\pi V_g}{\Phi_0}$.

The second equation in Eq. (B6) is differentiated with respect to the time and, plugging the second expression of Eq. (B5) in, we obtain

$$\ddot{\varphi}_I = -2 \frac{8E_C}{\hbar^2} [E_{J2} \sin(\varphi_g) - E_{J1} \sin(\varphi_I - \varphi_g)] \quad (\text{B8})$$

If we now consider identical junctions, i.e. $E_{J1} = E_{J2} = E_J$

$$\ddot{\varphi}_I = -2 \frac{8E_C E_J}{\hbar^2} [\sin \varphi_I - \sin(\varphi_g - \varphi_I)], \quad (\text{B9})$$

and exploiting $\sin(A) - \sin(B) = 2 \cos\left(\frac{A+B}{2}\right) \sin\left(\frac{A-B}{2}\right)$ we end up with the second order differential equation for the phase $\varphi_\Delta = \varphi_I - \frac{\varphi_g}{2}$

$$\ddot{\varphi}_\Delta = -2\Omega_J^2 \cos\left[\frac{\varphi_g(t)}{2}\right] \sin \varphi_\Delta, \quad (\text{B10})$$

where $\Omega_J = \frac{\sqrt{8E_C E_J}}{\hbar}$ is the Josephson frequency.

Taking the dimensionless variable $\tau = \frac{\omega_g}{2}t$, the derivatives with respect to the time become $\frac{\partial}{\partial t} = \frac{\omega_g}{2} \frac{\partial}{\partial \tau}$ and $\frac{\partial^2}{\partial t^2} = \frac{\omega_g^2}{4} \frac{\partial^2}{\partial \tau^2}$. This change of variable in Eq. (6) gives us the dimensionless differential equation

$$\frac{\partial^2 \varphi_\Delta}{\partial \tau^2} = -\bar{\epsilon} \cos(\tau) \sin \varphi_\Delta, \quad (\text{B11})$$

where

$$\bar{\epsilon} = 8 \frac{\Omega_J^2}{\omega_g^2} = \frac{64 E_C E_J}{(2e)^2 V_g^2}. \quad (\text{B12})$$

Appendix C: Derivation of the dissipative equation of motion

Let us derive the dissipative equation of motion for the superconductive phase using the resistively and capacitively shunted junction (RCSJ) model, where a Josephson junction is placed in parallel, as the name suggest, a capacitor and a resistor to approximate loss mechanisms in the junction. To this end, we utilize the two Josephson relations

$$I = I_C \sin \delta, \quad (\text{C1a})$$

$$\frac{\partial \delta}{\partial t} = \frac{2eV}{\hbar}, \quad (\text{C1b})$$

where I_C is the critical current, δ the superconducting phase difference across the junction, and V the voltage across the junction.

For both JJs in our circuit, the current through them is

$$I_j = I_C \sin \delta_j + C_j \frac{dV_j}{dt} + \frac{V_j}{R_j}, \quad (\text{C2})$$

$j \in \{g, I\}$. Using the second Josephson relation, Eq. (C1b), we can reformulate the equation for the current through the junction as

$$I_j = I_C \sin \delta_j + \frac{\hbar}{2e} C_j \frac{\partial^2 \delta}{\partial t^2} + \frac{\hbar}{2e R_j} \frac{\partial \delta}{\partial t}. \quad (\text{C3})$$

Let us write the phase differences across the junctions using the explicit node phases so that $\delta_1 = \varphi_g - \varphi_I$ and $\delta_2 = \varphi_I - \varphi_o$. The two JJs are in series, so the electric current through them must be equal

$$\begin{aligned} & I_C \sin(\varphi_g - \varphi_I) + \frac{\hbar}{2e} C_{J1} (\ddot{\varphi}_g - \ddot{\varphi}_I) + \frac{\hbar}{2e R_1} (\dot{\varphi}_g - \dot{\varphi}_I) \\ &= I_C \sin(\varphi_I - \varphi_o) + \frac{\hbar}{2e} C_{J2} (\ddot{\varphi}_I - \ddot{\varphi}_o) + \frac{\hbar}{2e R_2} (\dot{\varphi}_I - \dot{\varphi}_o). \end{aligned} \quad (\text{C4})$$

We note that node 3 is grounded, i.e. $\varphi_o = \dot{\varphi}_o = \ddot{\varphi}_o = 0$, and due to the voltage source in the circuit the phase

of node 2 satisfies

$$\varphi_g = \varphi_g(0) + \frac{2\pi}{\phi_0} V_g t, \quad (\text{C5a})$$

$$\dot{\varphi}_g = \frac{2\pi}{\phi_0} V_g = \omega_g. \quad (\text{C5b})$$

Assuming identical junctions with $R_1 = R_2 = R$ and recalling that the critical current relates to the Josephson energy so that $I_C = \frac{2\pi}{\phi_0} E_J$, we can solve Eq. (C4) to obtain

$$\begin{aligned} \ddot{\varphi}_I &= \frac{1}{\hbar^2} \frac{4e^2}{C_{J1} + C_{J2}} E_J [\sin(\varphi_I - \varphi_g) + \sin(\varphi_I)] \\ &+ \frac{1}{R(C_{J1} + C_{J2})} (-2\dot{\varphi}_I + \dot{\varphi}_g). \end{aligned} \quad (\text{C6})$$

Following the treatment of the EOM in Appendix B, we obtain

$$\ddot{\varphi}_\Delta = -2\Omega_J^2 \sin \varphi_\Delta \cos \frac{\varphi_g}{2} - \frac{2}{R(C_{J1} + C_{J2})} \dot{\varphi}_\Delta, \quad (\text{C7})$$

where $\frac{2}{R(C_{J1} + C_{J2})}$ is the dissipation rate. Writing this in dimensionless form, once again following the conventions of Appendix B, we recover Eq. (6) of the main text

$$\ddot{\varphi}_\Delta = -\bar{\epsilon} \cos(\tau) \sin \varphi_\Delta - \gamma \dot{\varphi}_\Delta \quad (\text{C8})$$

with $\gamma = \frac{2}{\omega_g} \frac{2}{R(C_{J1} + C_{J2})}$.

Appendix D: Computational methods

A code written in Julia environment is used for the numerical simulation of Eq. (C8), corresponding to Eq. (6) in the main text. The timespan of the integration is long in order for the dissipation to take place and eventually stabilize the solutions. Once the trajectory is obtained, the data related to the intermediate transient time are discarded, highlighting only the behavior of the trajectory in the long time regime, where its specific attractor shows up.

The classification in terms of attractors of the solutions is based on the threshold values $\varphi_{th} = 10^{-2}$ and $\dot{\varphi}_{th} = 5 \cdot 10^{-3}$ for the phase and its derivative, by means of the following criteria:

- π -stable : a solution for which $|\max \varphi_\Delta - \pi| < \varphi_{th}$ and $|\max \dot{\varphi}_\Delta| < \dot{\varphi}_{th}$;
- 0-stable: a solution for which $|\max \varphi_\Delta - 0| < \varphi_{th}$ and $|\max \dot{\varphi}_\Delta| < \dot{\varphi}_{th}$;
- cycle limit: a solution for which $|\max \varphi_\Delta - \pi| < \frac{\pi}{2}$ (or $|\max \varphi_\Delta| < \frac{\pi}{2}$ for limit-cycles around the downward fixed point) and $|\max \dot{\varphi}_\Delta| > \dot{\varphi}_{th}$;
- unstable: a solution for which $|\max \varphi_\Delta| > 2\pi$.

The space of the parameter we analyze is composed by points $(\varphi_{\Delta}(0), \bar{\epsilon})$, where $\varphi_{\Delta}(0) \in [\frac{\pi}{2}, \pi]$ and $\bar{\epsilon} \in [0.01, 0.6]$. Since in the beginning the space of the parameter under analysis is a grid of $1024 \times 1024 \sim 10^6$ solutions, we utilize an optimized computational method. In the first step we take just the extremal values of the parameters in their interval of definition, in such a way that we have 4 couples of point $(\varphi_{\Delta}, \bar{\epsilon})$ or, in other words, a space of the parameters of 2×2 classified solutions. In the second step, we bisect the interval for each parameter, generating a 3×3 space in which one quarter of the simulations comes from the previous 2×2 case, and the remaining ones need to be computed. This bisection scheme is repeated up to the final result of a map composed by 1024×1024 solutions. Here, we computed the fractal dimension of the regions generated by the four different attractors by means of the box counting method. Due to the discreteness of the points in the map, the Hausdorff's dimension is estimated via linear fits, see Fig. 4.

Again, the bisection scheme is implemented on the map's portion corresponding to the parameters $\bar{\epsilon} \in [0.3, 0.58]$ and $\varphi_{\Delta}(0) \in [0.5\pi, \pi]$, reported in Fig. 3a.

Here, limit-cycle solutions emerge. This kind of solution, after a transient time due to the dissipation, are trapped in stable and regular trajectories around $\varphi_{\Delta} = \pi, 0$. In our case, the limit-cycles are labelled in yellow in the map in Fig. 3a, while in Figs. 6-9 the phase-space portraits of four different limit-cycles are shown.

As an example, we analyze the trajectory in Fig. 6,

which nodes once on the left and once on the right side of the point $\varphi_{\Delta} = \pi$. Again, we recall that we define this specific case as a 1-cycle, where we call n -cycle a limit cycle trajectory with n nodes on each side, $2n$ in total, for every periodic oscillation. Furthermore, among the limit-cycle solutions we find complex and unusual trajectories, as 5-cycle and 9-cycle (see Figs. 8-9).

Following these results, the cycle-limit solutions found in this portion of the parameters space are further classified in terms of number of nodes $2n$ using the following procedure. First, we estimate the period of the regular orbit by means of the analysis of the component in frequency space, i.e. through the peaks of the Discrete Fourier Transform of $\varphi_{\Delta}(t) - \bar{\varphi}_{\Delta}$, where $\bar{\varphi}_{\Delta}(t)$ is the mean value of the phase: the smallest positive frequency ω^* is inverted for the determination of the period $T^* = \frac{2\pi}{\omega^*}$. The number of nodes is then determined by counting the times in which the velocity $\dot{\varphi}_{\Delta}(t)$ crosses the $\dot{\varphi} = 0$ axis in one period T^* . The results of the classification are reported in Figs. 3b-3d, where each limit-cycle solution is labelled by its number of nodes. In particular, it is possible to identify three main subregions with 1-cycle, 3-cycle and 5-cycle solutions, with 2, 6 and 10 nodes, respectively. However, narrow stripes of limit-cycles solutions with higher numbers of nodes occur for some specific values of the parameter $\bar{\epsilon}$, as reported in Figs. 3c-3d. For instance, in a neighborhood of $\bar{\epsilon} = 0.385$ a large band of 9-cycle solutions appears, while for $\bar{\epsilon} = 0.354838865, 0.361176755$ narrow stripes appear. The distribution of numbers of nodes for the band emerging for $\bar{\epsilon} = 0.354838865$ is reported in Fig. 5.

-
- [1] G. Wendin, Rep. Prog. Phys. **80**, 106001 (2017).
 [2] F. Arute, et al., Nature **574**, 505 (2019).
 [3] G. Q. AI, et al., Nature **614**, 676 (2023).
 [4] J. E. Mooij, et al., Science **285**, 1036 (1999).
 [5] J. M. Martinis, et al., Phys. Rev. Lett. **89**, 117901 (2002).
 [6] J. Koch, et al., Physical Review A **76**, 042319 (2007).
 [7] S. M. Girvin, Quantum machines: measurement and control of engineered quantum systems pp. 113–256 (2014).
 [8] Y. Aharonov and D. Bohm, Physical Review **115**, 485 (1959).
 [9] J. Kohlmann and R. Behr (2011).
 [10] J. P. Pekola, et al., Rev. Mod. Phys. **85**, 1421 (2013).
 [11] P. L. Kapitza, Sov. Phys. JETP **21**, 588 (1951).
 [12] D. Acheson, Proceedings of the Royal Society of London. Series A: Mathematical and Physical Sciences **448**, 89 (1995).
 [13] U. Vool and M. Devoret, International Journal of Circuit Theory and Applications **45**, 897 (2017).
 [14] W. C. Stewart, Applied Physics Letters **12**, 277 (1968).
 [15] M. Steffen, et al., Physical Review Letters **97**, 050502 (2006).
 [16] A. Stephenson, The London, Edinburgh, and Dublin Philosophical Magazine and Journal of Science **15**, 233 (1908).
 [17] M. Bartuccelli, G. Gentile, and K. Georgiou, Proceedings of the Royal Society of London. Series A: Mathematical, Physical and Engineering Sciences **457**, 3007 (2001).
 [18] D. E. Stewart, The ANZIAM Journal **42**, 451 (2001).